



A simplified finite strain plasticity model for metallic applications

Yiwei Chen¹ · Bassam A. Izzuddin¹

Received: 1 December 2022 / Accepted: 13 May 2023 / Published online: 9 June 2023
© The Author(s) 2023

Abstract

In this work, a finite strain elastoplastic model is proposed within a total Lagrangian framework based on multiplicative decomposition of the deformation gradient, with several simplifications aimed at facilitating more concise code implementation and enhancing computational efficiency. Pre- and post-processors are utilised for conversion between different stress and strain measures, sandwiching the core plastic flow algorithm which preserves the small strain form. Simplifications focus on the pre- and post-processor components by substituting certain arithmetic operations associated with high computational demands with simpler ones without compromising accuracy. These modifications are based on assumptions, which are valid for most metals, that the elastic strains are small compared to plastic strains, and that the incremental plastic deformations are small for each step. In addition, the consistent tangent modulus matrix is derived in a reduced form, both for the general full model and the new simplified model, facilitating more straightforward computations in both cases. The models are verified against two classical numerical examples where favourable comparisons are achieved. Overall, the simplified model is shown to provide a significant reduction in computational demand for the two considered numerical problems, with negligible deviation in the results compared to the full model, subject to fulfilling the underlying assumptions with the adoption of a sufficiently small step size.

Keywords Multiplicative decomposition · Total Lagrangian framework · Finite strain plasticity · Consistent tangent stiffness

1 Introduction

Finite strain plasticity is present in many engineering procedures and physical phenomena, such as metal forming and ductile fracture, which requires accurate constitutive modelling to capture geometric and material nonlinearity at large deformations. Unlike hyperelasticity which is characterised by a single constitutive relation, elasto-plasticity entails combined features from the distinct elastic and plastic responses, which are associated with many debates concerning their proper kinematic decomposition in the range of finite strains [1]. Depending on the means of separating elastic and plastic deformation (rate), current prevalent large strain elastoplasticity models fall into one of three main categories: (i) hypoelasto-plastic models which additively decompose the total rate of deformation tensor [2–5];

(ii) hyperelasto-plastic models based on the multiplicative decomposition of the total deformation gradient [6–11]; and (iii) elastoplastic models based on direct additive decomposition of the Seth–Hill family strains [12–14]. Apart from these, a type of model employing the plastic metric tensor as internal variables was also proposed for the general anisotropic material [15, 16]. A detailed review and comparison of these models can be found in [1, 17–19].

The classical hypoelasto-plastic formulation is set in the Eulerian framework and adopts an incremental structure similar to the infinitesimal strain plasticity. To fulfil frame indifference, it links a particular objective stress rate, with the rate of elastic deformation via a fourth-order elasticity tensor, where a variety of rate type were proposed and compared [20, 21]. Co-rotational rates such as the Zaremba–Jaumann rate was once considered as the optimal candidate as they fulfil the consistency condition initially established by Prager [22], which states that the yield surface must remain stationary with vanishing stress rate. Although simple in form, it was later discovered that the use of Jaumann rate causes an oscillatory stress response under simple shear

✉ Yiwei Chen
yiwei.chen16@imperial.ac.uk

¹ Department of Civil and Environmental Engineering,
Imperial College London, London, UK

mode [23]. To overcome this, other objective stress rates such as the Green–Naghdi rate were proposed. It has also been reported in general that the hypoelastic algorithm can induce spurious dissipation which leads to unrealistic non-repeated loops under cyclic loading [19]. Similarly, residual stresses were observed for completely closed elastic strain cycles [24]. As pointed out in [25], these issues were due to the non-exact integrability of the rate form of hypoelastic model to the hyperelastic relationships which incurs spurious dissipation. The requirement for objective rates to fulfil exact integrability is termed as the ‘elastic integrability criterion’ [1]. The need for a solution of this problem encouraged the development of the so-called self-consistent Eulerian model, where the unique logarithmic stress rate was discovered to fulfil Bernstein integrability condition [3]. Notably, the rate of elastic deformation was proved to be the same rate form of the Eulerian logarithmic strain; thus, the self-consistent Eulerian model can bypass the integrability issue and retain the simple additive constitutive structure. Despite these advantages, the model was later shown to fail to satisfy the weak-invariance requirement [26] and seemingly applicable only for linear or piecewise linear elastic relationship [27], with the former disadvantage posing a restriction on the choice of the reference configuration for the model. Accordingly, based on the above, it seems that all types of objective rates suffer from issues preventing them from being applicable to the most general material response.

The hyperelasto-plastic model is based upon Kröner–Lee’s decomposition of the total deformation gradient tensor [28], which facilitates the development of a numerical framework that circumvents the above-mentioned problems. The multiplicative decomposition leads to an additional intermediate configuration that is physically motivated from the theory of crystal plasticity. In addition, following the kinematic decomposition, the model directly employs a hyperelastic model fulfilling the frame indifference principle in terms of total form of stresses and strains, hence avoiding the use of incrementally objective integration algorithm [29] as in the case of hypoelastic model. It was also shown that model of this type fulfils the weak invariance [26]. Relevant pioneering work on theories and numerical implementation were attributed to Simo and his co-workers [8, 18, 30–32]. The framework was constructed based on the quadratic deformation tensors in either spatial or referential configuration with much complexity in terms of the return mapping and internal variable update procedure. Subsequent research [6, 7] constructed the model based on the intermediate configuration characterised by the Lagrangian logarithmic strain and an exponential update of the plastic deformation gradient tensor, though, despite a simpler structure, this is only restricted to moderate elastic strain cases. Recently, a new kinematic framework based on the concept of elastic strain corrector was proposed in

[33] and subsequently extended to incorporate nonlinear kinematic hardening [27] and plane stress constraints [11] amongst other features. The framework was derived via the chain rule obtained from the equivalent infinitesimal strain counterpart, and it can be applied to cases with anisotropy, large elastic strain, and nonzero plastic spin.

Models belonging to the third class also share the common constitutive structure as the hyperelasto-plastic model, except that they adopt an additive decomposition of the non-linear strains and hence an additive update of internal variables. Originally proposed by Green and Naghdi [12], the framework was later generalised by Papadopoulos and Lu [34] to the full Seth–Hill family strains. This type of model can produce comparable results with those obtained from the multiplicative decomposition model in analysis without significant non-coaxial deformation, normally with a simpler algorithmic structure. However, it is demonstrated in [33] that under the assumption of small elastic strain and perfectly plastic material, additive strain decomposition models, as opposed to multiplicative decomposition, are generally incapable of generating a constant shear stress corresponding to increasing shear strain. Among all types of strains, logarithmic strain performs relatively well in the analysis, and since its definition reflects the true relative deformation, this is normally adopted as the strain measure superior to others in the additive decomposition model. Still in general, these models fail to satisfy the weak invariance [26] and lead to a loss of ellipticity for deformation under non-coaxial loading [35] as well as softening and localisation of deformation at excessive strains [14].

All the aforementioned models attempt to recover the infinitesimal strain elastoplasticity constitutive structure in the range of large deformations via different kinematic decomposition measures, and indeed, this consideration usually contributes to the complexity and high numerical cost of the algorithm. In this paper, we adopt the isotropic hyperelasto-plastic model with logarithmic strain in a total Lagrangian Finite Element framework, and we propose several further simplifications to the kinematic relationship under the assumptions of small elastic deformation and small incremental plastic deformations. The resulting simplified model would have combined kinematic features from Kröner–Lee decomposition and Papadopoulos–Lu decomposition, enabling the model structure to get closer to the classical infinitesimal strain model. We also propose a formulation for the consistent tangent modulus which can be computed in the reduced second-order tensor form with lower computational effort compared to existing formulations. With the focus on the geometric pre- and post-processors, standard elastic and plastic constitutive relationships are considered, adopting the Hecky’s hyperelastic model and the von Mises yield criterion. The remainder of the paper is structured as follows. In Sects. 2 and 3, the continuum formulation and

implementation of the full consistent model are reviewed, while Sect. 4 presents the main simplifications proposed in the current work. These are followed in Sect. 5 by the derivation of consistent tangent stiffness for both the full and simplified models. Finally, the accuracy and efficiency of the simplified formulation are assessed in the context of quasi-static and dynamic analysis using two classical numerical examples from finite strain plasticity literature.

2 Full continuum model formulation

2.1 Kinematics

Consider a continuum body Ω in 3D Euclidean space \mathbb{R}^3 with prescribed traction boundary $\partial\Omega_t$ and prescribed displacement boundary $\partial\Omega_u$ with $\partial\Omega_t \cap \partial\Omega_u = 0$. Let the reference configuration coincide with its natural undeformed state and described by the material coordinates \mathbf{X} . Assume the body undergoes certain motion over some time interval of interest described by the deformation mapping $\phi(\mathbf{X}, t)$, and the deformed body occupies the spatial configuration with spatial coordinates \mathbf{x} . The deformation gradient tensor is then defined in a material pointwise manner as:

$$\mathbf{F}(\mathbf{X}, t) = \frac{\partial \mathbf{x}(\mathbf{X}, t)}{\partial \mathbf{X}} = \nabla \phi(\mathbf{X}, t) \tag{1}$$

Kröner–Lee’s decomposition then splits the total deformation gradient tensor into elastic and plastic parts via a multiplicative operation, dropping henceforth the spatial and temporal arguments:

$$\mathbf{F} = \mathbf{F}_e \mathbf{F}_p \tag{2}$$

Equation (2) introduces an unstressed intermediate configuration described by \mathbf{F}_p that could be achieved by artificially removing all stresses. In this case, the elastic deformation gradient tensor \mathbf{F}_e characterises stretching and rigid body motion of crystals, whereas the plastic deformation gradient \mathbf{F}_p corresponds to dislocation flow between crystal layers [36] which is volume preserving, i.e. $J_p = \det(\mathbf{F}_p) \equiv 1$. Additionally, rotation of the intermediate configuration is ambiguous as an arbitrary rotation tensor can be inserted into Eq. (2) without affecting the decomposition, i.e. $\mathbf{F} = \mathbf{F}_e \mathbf{F}_p = \mathbf{F}_e \mathbf{Q}^T \mathbf{Q} \mathbf{F}_p$. In some early literature [37], uniqueness of the decomposition is enforced by including all rigid body rotation in the plastic part, and the elastic deformation gradient only consists of the left stretch part \mathbf{V}_e . For isotropic material, this rotation does not affect the stress measures defined in the reference and spatial configuration, which are considered to be ‘structural frame invariant’ [36]. As shown later, this property can be employed to facilitate numerical

implementation with a reduced storage requirement by only storing the stretch part of the plastic deformation gradient tensor in Voigt form.

Next, given the velocity gradient tensor \mathbf{L} , its symmetric and skew-symmetric part is defined as the rate of deformation tensor \mathbf{D} and the spin tensor \mathbf{W} , respectively:

$$\mathbf{L} = \dot{\mathbf{F}}\mathbf{F}^{-1} \tag{3}$$

$$\mathbf{D} = \text{sym}(\mathbf{L}) = \frac{1}{2}(\dot{\mathbf{F}}\mathbf{F}^{-1} + \mathbf{F}^{-T}\dot{\mathbf{F}}^T) \tag{4}$$

$$\mathbf{W} = \text{skw}(\mathbf{L}) = \frac{1}{2}(\dot{\mathbf{F}}\mathbf{F}^{-1} - \mathbf{F}^{-T}\dot{\mathbf{F}}^T) \tag{5}$$

Their elastic and plastic counterparts follow straightforwardly from the multiplicative decomposition Eq. (2). The plastic spin is generally assumed to be zero, representing the irrotational plastic flow. Modifications accounting for finite plastic spin were also proposed by involving an additional rotation stage applied to the final outcome [9].

$$\mathbf{L}_e = \dot{\mathbf{F}}_e \mathbf{F}_e^{-1} \quad \mathbf{L}_p = \dot{\mathbf{F}}_p \mathbf{F}_p^{-1} \tag{6}$$

$$\mathbf{D}_e = \frac{1}{2}(\dot{\mathbf{F}}_e \mathbf{F}_e^{-1} + \mathbf{F}_e^{-T} \dot{\mathbf{F}}_e^T) \quad \mathbf{D}_p = \frac{1}{2}(\dot{\mathbf{F}}_p \mathbf{F}_p^{-1} + \mathbf{F}_p^{-T} \dot{\mathbf{F}}_p^T) \tag{7}$$

$$\mathbf{W}_e = \frac{1}{2}(\dot{\mathbf{F}}_e \mathbf{F}_e^{-1} - \mathbf{F}_e^{-T} \dot{\mathbf{F}}_e^T) \quad \mathbf{W}_p = \frac{1}{2}(\dot{\mathbf{F}}_p \mathbf{F}_p^{-1} - \mathbf{F}_p^{-T} \dot{\mathbf{F}}_p^T) \tag{8}$$

Since the elastic and plastic quantities are defined relative to different configurations, to achieve an additive relationship in spatial configuration, the plastic velocity gradient needs to be pushed forward. This indirect additive relationship is central to the distinction between hyper- and hypoelasto-plastic models:

$$\mathbf{L} = \mathbf{L}_e + \mathbf{F}_e \mathbf{L}_p \mathbf{F}_e^{-1} \tag{9}$$

Finally, two main strain measures used in the constitutive relationship and the 3D continuum finite element framework, respectively, are defined below. Evaluation of the Lagrangian logarithmic strain defined in the intermediate configuration requires a spectral decomposition on the right Cauchy deformation tensor $\mathbf{C} = \mathbf{F}^T \mathbf{F}$ as:

$$\bar{\mathbf{E}} = \frac{1}{2} \ln(\mathbf{C}) = \sum_{i=1}^3 \ln(\lambda_i) \mathbf{N}_i \otimes \mathbf{N}_i \tag{10}$$

where $\bar{\mathbf{E}}$ is the logarithmic strain, λ_i is the i th principal stretch, and \mathbf{N}_i is the corresponding principal direction defined in the unrotated configuration. On the other hand, the strain measure in the reference configuration, hence used in the Total Lagrangian framework, is the Green strain that is defined by a simpler linear relationship with the deformation tensor:

$$\mathbf{E} = \frac{1}{2}(\mathbf{C} - \mathbf{I}) = \sum_{i=1}^3 \frac{1}{2}(\lambda_i^2 - 1)\mathbf{N}_i \otimes \mathbf{N}_i \quad (11)$$

2.2 Constitutive equations

Following the two laws of thermodynamics under isothermal condition, the non-negative dissipation can be expressed as the difference between stress power and the rate of change of free energy:

$$\mathcal{D}_p = P - \dot{\psi} \geq 0 \quad (12)$$

where \mathcal{D}_p is the plastic dissipation, \mathcal{P} is the stress power, and ψ is the free energy density. In this case, it is assumed that all quantities are evaluated in the intermediate configuration. The exact form of the stress power can be derived from the current configuration using Eq. (9), starting from the work conjugate pair of Kirchhoff stress $\boldsymbol{\tau}$ and velocity gradient \mathbf{L} and applying pull backwards operations to both stress and deformation rate [9]. Alternatively, it may also be derived via the microscopic virtual power balance [35]. For subsequent development, the former approach is followed.

$$\begin{aligned} \boldsymbol{\tau} : \mathbf{L} &= \boldsymbol{\tau} : (\mathbf{L}_e + \mathbf{F}_e \mathbf{L}_p \mathbf{F}_e^{-1}) = \mathbf{F}_e^{-1} \boldsymbol{\tau} \mathbf{F}_e^{-T} : \mathbf{F}_e^T (\mathbf{L}_e + \mathbf{F}_e \mathbf{L}_p \mathbf{F}_e^{-1}) \mathbf{F}_e \\ &= \mathbf{S}_e : (\mathbf{F}_e^T \mathbf{L}_e \mathbf{F}_e + \mathbf{C}_e \mathbf{L}_p) = \mathcal{P}_e + \mathcal{P}_p \end{aligned} \quad (13)$$

where \mathbf{S}_e is the elastic second Piola–Kirchhoff stress, \mathbf{C}_e is the elastic right Cauchy deformation tensor, \mathcal{P}_e and \mathcal{P}_p are elastic and plastic stress power, respectively. One can interpret the former two quantities in analogy with treating the intermediate configuration as the reference configuration and elastic deformation as total deformation. Since elastic second Piola–Kirchhoff stress is symmetric, from Eq. (13), its conjugate pair strain rate can be derived from stretch rate as the elastic Green strain rate $\dot{\mathbf{E}}_e$, while there is no associated stress power expended on rotation since elastic spin is skew symmetric:

$$\mathcal{P}_e = \mathbf{S}_e : \mathbf{F}_e^T \mathbf{L}_e \mathbf{F}_e = \mathbf{S}_e : \mathbf{F}_e^T \mathbf{D}_e \mathbf{F}_e = \mathbf{S}_e : \dot{\mathbf{E}}_e \quad (14)$$

where the elastic Green strain is defined as:

$$\mathbf{E}_e = \frac{1}{2}(\mathbf{F}_e^T \mathbf{F}_e - \mathbf{I}) \quad (15)$$

To facilitate elastic constitutive model specification, the elastic stress power could be replaced by other work conjugate pairs. As Hencky's model is formulated in terms of logarithmic strain, Eq. (14) is re-expressed by pushing forward to the stretched and unrotated configuration, noting that such kinematic transformation is only valid for isotropic materials:

$$\mathbf{S}_e : \dot{\mathbf{E}}_e = \mathbf{U}_e \mathbf{S}_e \mathbf{U}_e : \mathbf{U}_e^{-1} \dot{\mathbf{E}}_e \mathbf{U}_e^{-1} = \bar{\boldsymbol{\tau}} : \dot{\bar{\mathbf{E}}}_e \quad (16)$$

The rotated Kirchhoff stress can also be interpreted as the Kirchhoff stress in spatial configuration being rotated back by the amount corresponding to elastic rotation tensor:

$$\bar{\boldsymbol{\tau}} = \mathbf{R}_e^T \boldsymbol{\tau} \mathbf{R}_e \quad (17)$$

On the other hand, the plastic power can be rearranged in terms of the unsymmetric Mandel stress work conjugate to the plastic velocity gradient in the intermediate configuration:

$$\mathcal{P}_p = \mathbf{S}_e : \mathbf{C}_e \mathbf{L}_p = \mathbf{M}_e : \mathbf{L}_p \quad (18)$$

where the Mandel stress is defined as:

$$\mathbf{M}_e = \mathbf{C}_e \mathbf{S}_e = \mathbf{F}_e^T \boldsymbol{\tau} \mathbf{F}_e^{-T} \quad (19)$$

The transformation rule renders the Mandel stress as a mixed-variant stress tensor rather than contravariant tensor [15]. In general, the property of asymmetry leads to the unconventional nine-dimensional plastic flow rule for both rate of plastic deformation and plastic spin tensor. However, due to the assumption of elastic isotropy, the elastic second Piola–Kirchhoff tensor and the elastic Cauchy deformation tensor commute. The skew-symmetric part of Mandel stress thus becomes zero, whereas the symmetric part coincides with the rotated Kirchhoff stress; thus,

$$\mathcal{P}_p = \bar{\boldsymbol{\tau}} : \mathbf{D}_p \quad (20)$$

Substituting Eqs. (16) and (20) into the dissipation inequality (12) gives the dissipation rule for isotropic elastoplastic material under the isothermal assumption:

$$\mathcal{D}_p = \bar{\boldsymbol{\tau}} : \dot{\bar{\mathbf{E}}}_e + \bar{\boldsymbol{\tau}} : \mathbf{D}_p - \dot{\psi} \geq 0 \quad (21)$$

The free energy density is composed of contributions from both elastic ψ_e and plastic ψ_p parts. The latter is also termed as defect energy accounting for hardening effect and, within the pure mechanical framework, whether it is regarded as a dissipative part or not has no influence on the constitutive laws derived [35]. By the standard Coleman–Noll procedure, the elastic stress relation and the reduced dissipation inequality can be derived assuming arbitrary pure elastic or plastic deformation rate. Assuming that the elastic free energy is formulated directly in terms of the elastic logarithmic strain, then from Eq. (21):

$$\begin{cases} \bar{\boldsymbol{\tau}} = \frac{\partial \psi_e}{\partial \bar{\mathbf{E}}_e} \\ \mathcal{D}_p = \bar{\boldsymbol{\tau}} : \mathbf{D}_p - \dot{\psi}_p \geq 0 \end{cases} \quad (22)$$

The hyperelastic model employed in this work is the Hencky model which is a direct extension of the small

strain isotropic elastic model to the finite strain range based on the logarithmic strain. The model is able to predict the nonlinear hyperelastic response up to a stretch of around 1.5, which suffices for metal applications [38]. Similar to its small strain counterpart, the free energy form has the volumetric and deviatoric part as shown below in full strain space:

$$\psi_e = U(J_e) + W(\bar{\mathbf{E}}_e) = \frac{1}{2}K\ln(J_e)^2 + \mu DEV(\bar{\mathbf{E}}_e) : DEV(\bar{\mathbf{E}}_e) \tag{23}$$

where J_e is the elastic Jacobian equal to $\det(\mathbf{F}_e)$; K and μ are the bulk and shear moduli, respectively; and $DEV(\bar{\mathbf{E}}_e)$ is deviatoric component of the elastic logarithmic strains defined as:

$$DEV(\bar{\mathbf{E}}_e) = \bar{\mathbf{E}}_e - \frac{1}{3}tr(\bar{\mathbf{E}}_e) \tag{24}$$

The stress relation then follows from Eq. (22). In this case, since the evaluation of logarithmic strain requires spectral decomposition, it would be more convenient to determine the stress relation in eigenspace and convert back via the rotation tensor containing principal directions:

$$\bar{\tau}_i = \frac{\partial \psi_e}{\partial \bar{E}_{e,i}} = \frac{\partial \psi_e}{\partial \lambda_{e,i}} \frac{\partial \lambda_{e,i}}{\partial \bar{E}_{e,i}} = \lambda_{e,i} \frac{\partial \phi}{\partial \lambda_{e,i}} = 2\mu \left(\ln \lambda_{e,i} - \frac{1}{3} \ln J_e \right) + K \ln(J_e) \tag{25}$$

where $\lambda_{e,i}$ is the i th principal elastic stretch and $\bar{E}_{e,i}$ is the i th principal elastic logarithmic strain.

On the other hand, the plastic flow rule and internal variable evolution laws can be derived from the reduced dissipation inequality via the principle of maximum dissipation which also implies the convexity of the elastic domain. In this work, the classical von Mises yield function with nonlinear mixed hardening is adopted to constrain the admissible elastic space. Since we are concerned with a configuration which differs from the spatial configuration by the elastic rotation only, the same form of yield function can also be applied to the rotated Kirchhoff stresses. The classical formulation is shown below:

$$f(\bar{\boldsymbol{\xi}}, e_p) = \sqrt{DEV(\bar{\boldsymbol{\xi}}) : DEV(\bar{\boldsymbol{\xi}})} - \sqrt{\frac{2}{3}}(\sigma_{Y0} + R(e_p)) \tag{26}$$

where $\bar{\boldsymbol{\xi}}$ is the relative stresses defined as the difference between the rotated Kirchhoff stresses and the back stresses in intermediate configuration, σ_{Y0} is the initial yield stress at zero equivalent plastic strain, e_p is the equivalent logarithmic plastic strain, and R is the incremental yield stress accounting for isotropic hardening.

The maximum dissipation principle states that given a plastic strain rate, among all admissible states bounded by the yield function, the actual stresses along with the

hardening stress-like variables must give rise to the maximum plastic dissipation as defined in Eq. (22). Thus, it can be treated as a constrained optimisation problem with the Lagrangian function defined below. The argument of the yield function has been changed to a general form to include all internal variables:

$$\min_{\{\bar{\tau}, R, \bar{\tau}_B, \gamma\}} - \mathcal{L}(\bar{\tau}, R, \bar{\tau}_B, \gamma) \tag{27}$$

$$L(\bar{\tau}, R, \bar{\tau}_B, \gamma) = \mathcal{D}_p(\bar{\tau}, R, \bar{\tau}_B) - \gamma f(\bar{\tau}, R, \bar{\tau}_B) \tag{28}$$

where $\bar{\tau}_B$ is the rotated Kirchhoff back stress; and γ is the Lagrangian multiplier and also termed as consistency parameter in the context of plasticity theorem. To completely define the reduced dissipation Eq. (22), the plastic free energy is assumed to depend on some strain-like measures accounting for isotropic and kinematic hardening separately. The corresponding thermodynamic stress-like variables are the incremental yield stress and back stress, respectively:

$$R = -\frac{\partial \psi_p}{\partial e_p}, \bar{\tau}_B = -\frac{\partial \psi_p}{\partial \mathbf{E}_B} \tag{29}$$

The rate form is thus the combination of thermodynamic work conjugate pairs of stress and strain rate internal variables:

$$\dot{\psi}_p(e_p, \mathbf{E}_B) = \frac{\partial \psi_p}{\partial e_p} \dot{e}_p + \frac{\partial \psi_p}{\partial \mathbf{E}_B} : \dot{\mathbf{E}}_B = -R \cdot \dot{e}_p - \bar{\tau}_B : \dot{\mathbf{E}}_B \tag{30}$$

The first-order necessary condition of the Lagrangian function Eq. (28) along with Eq. (30) for stationary points then leads to the plastic flow rule, internal strain-like variable evolution law, the Karush–Kuhn–Tucker inequalities, or loading/unloading conditions and convexity of the yield function. For metal applications, the flow rule is usually associative; otherwise, the direction of rate of plastic deformation would be determined by some plastic potential function.

$$\begin{cases} \mathbf{D}_p = \gamma \frac{\partial f(\bar{\tau}, e_p, \bar{\tau}_B)}{\partial \bar{\tau}} \\ \dot{e}_p = \gamma \frac{\partial f(\bar{\tau}, e_p, \bar{\tau}_B)}{\partial R} \\ \dot{\mathbf{E}}_B = \gamma \frac{\partial f(\bar{\tau}, e_p, \bar{\tau}_B)}{\partial \bar{\tau}_B} \\ \gamma \geq 0, f(\bar{\tau}, e_p, \bar{\tau}_B) \leq 0, \gamma f(\bar{\tau}, e_p, \bar{\tau}_B) = 0 \end{cases} \tag{31}$$

The back stress rate follows Prager’s rule and is directly proportional to the plastic strain rate, where a direct split of total hardening modulus is used to treat mixed hardening. For nonlinear hardening, the modulus is dependent on the equivalent plastic strain as hardening variable.

$$\dot{R} = A_i(e^p) \dot{e}_p, \dot{\bar{\tau}}_B = A_k(e^p) \dot{e}_p \mathbf{N}_p \tag{32}$$

$$A_i(e^p) + A_k(e^p) = A(e^p) \tag{33}$$

in which \mathbf{N}_p is direction of incremental plastic deformation, A is the total hardening modulus, A_i and A_k are isotropic and kinematic hardening modulus. Apart from these conditions, the consistency requirement on the rate of yield function must also be fulfilled when there is plastic flow:

$$\gamma > 0, \dot{f}(\bar{\boldsymbol{\tau}}, e_p, \bar{\boldsymbol{\tau}}_B) = 0 \quad (34)$$

Substituting the von Mises yield function into Eq. (30) gives the exact form of plastic flow rule and internal variable evolution law in our assumed case:

$$\begin{cases} \mathbf{D}_p = \gamma \mathbf{N}_p = \gamma \frac{\text{DEV}(\bar{\boldsymbol{\xi}})}{\|\text{DEV}(\bar{\boldsymbol{\xi}})\|} \\ \dot{e}_p = \sqrt{\frac{2}{3}} \gamma \\ \dot{\bar{\boldsymbol{\tau}}}_B = \frac{2}{3} A_k (e^p) \gamma \mathbf{N}_p = \frac{2}{3} A_k (e^p) \gamma \frac{\text{DEV}(\bar{\boldsymbol{\xi}})}{\|\text{DEV}(\bar{\boldsymbol{\xi}})\|} \end{cases} \quad (35)$$

3 Implementation of full model

Numerical implementation of the hyperelasto-plastic model resembles that of the infinitesimal strain case, with additional pre- and post-processors for kinematic transformations sandwiching the return algorithm. For the von Mises yield function, state update procedure takes the form of radial return mapping with backwards Euler integration of the flow rule and evolution laws. The state variable characterising the plastic deformation would be the symmetric right stretch part \mathbf{U}_p of \mathbf{F}_p obtained via polar decomposition $\mathbf{F}_p = \mathbf{R}_p \mathbf{U}_p$ for the reasons noted in Sect. 2. This allows storing the plastic deformation in the reduced Voigt form. Effectively for the converged iteration in each step, the internal variables are updated with respect to a configuration that is rotated away from the intermediate configuration represented by \mathbf{F}_p with a non-identity plastic rotation matrix. Such deviation increases with the magnitude of plastic rotation introduced by the non-coaxial plastic flow update procedure.

Assume a temporal discretisation over a specific time interval of interest $[t_0, \dots, t_n, \dots, t_e]$, and consider the current time step t_{n+1} , then it is required to find the second Piola–Kirchhoff stresses $\mathbf{S}^{t_{n+1}}$ and updated state variables $\{\mathbf{U}_p^{t_{n+1}}, e_p^{t_{n+1}}, \bar{\boldsymbol{\tau}}_B^{t_{n+1}}\}$ given Green strains at current time $\mathbf{E}^{t_{n+1}}$ and old state variables from previous time step t_n . In following presentation, the superscript t_{n+1} is dropped. The first step is to use a geometric pre-processor to obtain the trial elastic logarithmic strain assuming a frozen plastic flow. By multiplicative decomposition, the trial elastic deformation gradient tensor is:

$$\mathbf{F}_e^{\text{trial}} = \mathbf{F}(\mathbf{U}_p^{\text{trn}})^{-1} \quad (36)$$

where \mathbf{F} is the total deformation gradient tensor at current step; $\mathbf{U}_p^{\text{trn}}$ is the plastic stretch tensor in the previous step. The trial Cauchy deformation then follows as:

$$\mathbf{C}_e^{\text{trial}} = (\mathbf{F}_e^{\text{trial}})^T \mathbf{F}_e^{\text{trial}} = (\mathbf{U}_p^{\text{trn}})^{-1} (2\mathbf{E} + \mathbf{I})(\mathbf{U}_p^{\text{trn}})^{-1} \quad (37)$$

The logarithmic strain is then computed by the spectral decomposition on the trial deformation tensor:

$$\begin{aligned} \bar{\mathbf{E}}_e &= \sum_{i=1}^3 \frac{1}{2} \ln \left(\left(\lambda_{e,i}^{\text{trial}} \right)^2 \right) \mathbf{N}_i \otimes \mathbf{N}_i \\ &= \mathbf{Q}(\mathbf{N}_i) \mathbf{Diag} \left(\frac{1}{2} \ln \left(\left(\lambda_{e,i}^{\text{trial}} \right)^2 \right) \right) \mathbf{Q}(\mathbf{N}_i)^T \end{aligned} \quad (38)$$

where $\mathbf{Q}(\mathbf{N}_i)$ is the orthogonal rotation tensor containing principal directions as columns; $\mathbf{Diag}(\bullet)$ is the diagonal matrix containing principal strains. Afterwards, this is input into the standard return mapping algorithm to obtain updated stresses and state variables. As derived in [9], use of the logarithmic strain leads to the additive elastic and incremental plastic strain decomposition for moderate trial elastic strains. This renders classical return mapping feasible, and the justification is mainly attributed to the plastic flow rule Eq. (35). As the plastic spin is assumed to be zero and also does not participate in the dissipation, the plastic deformation increment is solely characterised by the symmetric part of the associated velocity gradient:

$$\mathbf{D}_p = \gamma \mathbf{N}_p = \mathbf{L}_p = \dot{\mathbf{F}}_p \mathbf{F}_p^{-1} \quad (39)$$

The backwards Euler integration of the ordinary differential equation Eq. (39) results in the exponential update of the plastic deformation gradient at current step:

$$\mathbf{F}_p = \exp(\Delta t \cdot \mathbf{D}_p) \mathbf{F}_p^{t_n} = \exp(\Delta \gamma \mathbf{N}_p) \mathbf{U}_p^{t_n} \quad (40)$$

It should be noted that if the exponential term is non-coaxial with the old plastic stretch, e.g. under a simple shear mode, the resulting new \mathbf{F}_p would be unsymmetric and some plastic rotation is induced. Substituting Eq. (40) into the multiplicative decomposition in Eq. (36) then gives the final elastic deformation gradient tensor at t_{n+1} :

$$\mathbf{F}_e = \mathbf{F} \mathbf{F}_p^{-1} = \mathbf{F}_e^{\text{trial}} \cdot \exp(-\Delta \gamma \mathbf{N}_p) \quad (41)$$

The additive relationship can then be derived by establishing the relationship between final and trial deformation tensors, where from Eqs. (37) and (41):

$$\mathbf{C}_e^{\text{trial}} = \exp(\Delta \gamma \mathbf{N}_p)^T \mathbf{C}_e \exp(\Delta \gamma \mathbf{N}_p) \quad (42)$$

The conversion from Eq. (42) to additive decomposition is indeed related to the exponential term approximation. Recalling that $\mathbf{C}_e^{\text{trial}} = \exp(2\bar{\mathbf{E}}_e^{\text{trial}})$ and $\mathbf{C}_e = \exp(2\bar{\mathbf{E}}_e)$, all the exponential terms can be expressed as Taylor expansions and retaining only the first-order terms yields the additive decomposition. Indeed, this relationship only holds for moderate trial elastic strain as well as incremental plastic deformation:

$$\bar{\mathbf{E}}_e^{\text{trial}} \approx \bar{\mathbf{E}}_e + \Delta\gamma \mathbf{N}_p \tag{43}$$

The radial return mapping determines the Lagrangian multiplier $\Delta\gamma$ through consistency condition in Eq. (34), where for nonlinear hardening a Newton iterative procedure is required to determine the parameter. The new internal variables are then updated through the incremental form of Eqs. (35) and (40):

$$\begin{cases} \bar{\boldsymbol{\tau}} = \text{DEV}(\bar{\boldsymbol{\tau}}^{\text{trial}}) - 2\mu\Delta\gamma\mathbf{N}_p + \frac{1}{3}\text{tr}(\bar{\boldsymbol{\tau}}^{\text{trial}}) \\ e_p = \sqrt{\frac{2}{3}}\Delta\gamma + e_p^n \\ \bar{\boldsymbol{\tau}}_B = \frac{2}{3}A_k(e^p)\Delta\gamma\mathbf{N}_p + \bar{\boldsymbol{\tau}}_B^n \end{cases} \tag{44}$$

In the geometric post-processor stage, the rotated Kirchhoff stresses are pulled backwards to the reference configuration by consecutive operations using the updated elastic and plastic deformation gradient tensors:

$$\mathbf{S} = \mathbf{F}_p^{-1}\mathbf{U}_e^{-1}\bar{\boldsymbol{\tau}}\mathbf{U}_e^{-1}\mathbf{F}_p^{-T} \tag{45}$$

noting that according to Eq. (41), the principal directions of the updated elastic stretch generally differ from those of the trial state, and also if kinematic hardening is used, then the final stress state is no longer coaxial with the trial elastic deformation.

For a small increment step size, Eq. (45) can be approximated with the trial elastic deformation gradient and the previous plastic deformation gradient. This can be reasoned since for small increment steps, the elastic rotation tensor is hardly distinct between the trial state and final state:

$$\mathbf{U}_e\mathbf{F}_p = \mathbf{R}_e^T\mathbf{F} = (\mathbf{R}_e^T\mathbf{R}_e^{\text{trial}})\mathbf{U}_e^{\text{trial}}\mathbf{U}_p^n \approx \mathbf{U}_e^{\text{trial}}\mathbf{U}_p^n \tag{46}$$

Hence, Eq. (45) can be replaced with:

$$\mathbf{S} \approx (\mathbf{U}_p^n)^{-1}(\mathbf{U}_e^{\text{trial}})^{-1}\bar{\boldsymbol{\tau}}(\mathbf{U}_e^{\text{trial}})^{-1}(\mathbf{U}_p^n)^{-1} \tag{47}$$

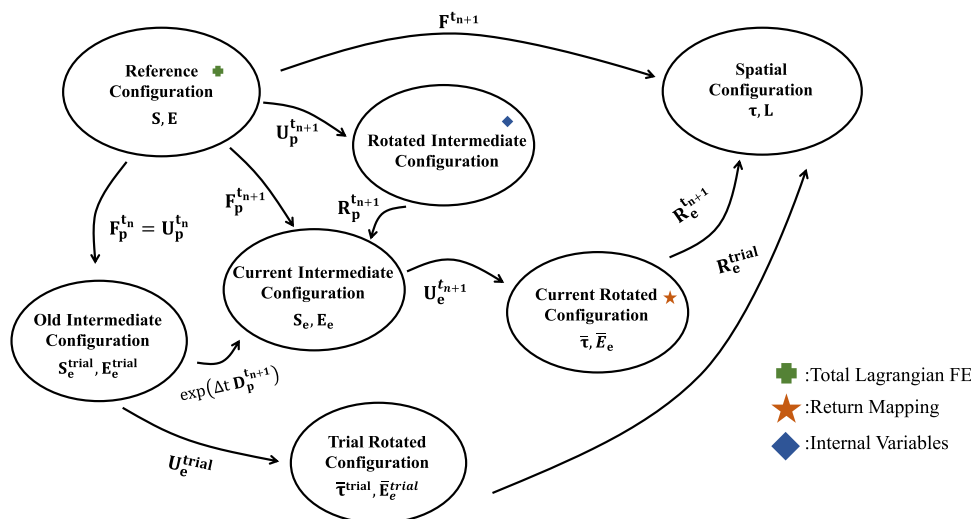
noting that the elastic trial stretch $\mathbf{U}_e^{\text{trial}}$ would need additional computation by spectral decomposition on $\mathbf{C}_e^{\text{trial}}$ or polar decomposition if $\mathbf{F}_e^{\text{trial}}$ is calculated.

Moreover, the intermediate configuration is rotated by \mathbf{R}_p determined from polar decomposition of the updated plastic deformation gradient, and all quantities associated with that configuration, including plastic deformation gradient and back stresses, undergo the same transformation. Note that since the updated back stresses before rotation correction are defined with respect to the current rotated configuration shown in Fig. 1, the new back stresses are determined by pulling backwards to rotated intermediate configuration and then push forwards to the new rotated configuration by new rotated elastic stretch $\mathbf{R}_p^T\mathbf{U}_e\mathbf{R}_p$; thus, overall, the back stress would also be rotated. Finally, for conceptual clarity, the configurations involved in the full model algorithm are shown in the Fig. 1.

4 Simplified model formulation

In this work, we simplify the geometric pre- and post-processor based on stricter assumptions posed on the magnitude of the trial elastic deformation and incremental plastic

Fig. 1 Configurations involved in the full consistent hyperelasto-plastic model, with important configurations highlighted with markers



deformation, because evaluation of the logarithmic strain and the exponential mapping update poses a relatively high computational demand. Such demand not only stems from the need for spectral decomposition but also from arithmetic operations of natural logarithm and exponential themselves. Under the first assumption mentioned above, the intermediate configuration would be hardly different from the rotated configuration. As a result, the trial elastic stretch U_e^{trial} would be close to an identity second-order tensor, and hence, the elastic deformation gradient tensor is dominated by the rotation component only, allowing insignificantly different configurations to be neglected. In the simplified model, when determining trial elastic strains, the logarithmic strain measure can be directly replaced by the elastic Green strains which has a linear relationship with the elastic deformation tensor, thus replacing Eq. (38) with:

$$E_e^{trial} = \frac{1}{2}(C_e^{trial} - I) \approx \bar{E}_e^{trial} = \frac{1}{2} \ln(C_e^{trial}) \quad (48)$$

The resulting hyperelastic model retains the infinitesimal strain form and is of St. Venant–Kirchhoff type, where Eq. (25) formulated in eigenspace is replaced by the triaxial form:

$$S_e = \left(K - \frac{2}{3} \mu \right) \text{tr}(E_e) I + 2 \mu E_e \approx \bar{\tau} \quad (49)$$

Such a hyperelastic model is well known for potential instability and unrealistic softening under a regime of significant compression [39]. However, with elastic strains encountered in typical engineering application of metallic structure, this would be a negligible concern, as demonstrated in subsequent numerical examples. Note that Eq. (48) still renders additive decomposition feasible, and it actually corresponds to the first-order Taylor series expansion of the

logarithmic strain. Figure 2 shows the reduced configurations based on the two assumptions.

Now the return mapping algorithm and hardening variables are also evaluated in the space of elastic second Piola–Kirchhoff stress and its power conjugate pair strain. Next in the post-processor module, transformation to the second Piola–Kirchhoff stress is achieved via a simpler relationship than Eq. (47). For the simplified model, only one pulling backwards operation is involved, which avoids the need for evaluating the trial elastic stretch which in turn poses additional computational demand:

$$S \approx (U_p^{tn})^{-1} S_e (U_p^{tn})^{-1} \quad (50)$$

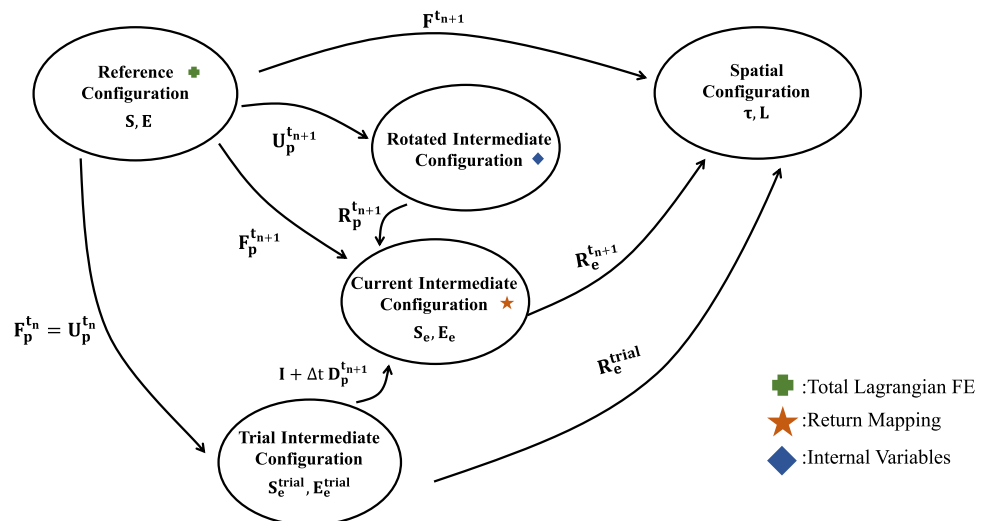
The exponential update procedure of the plastic deformation gradient can also simply be replaced by the truncated Taylor series expansion, leading to an additive update structure similar to the infinitesimal strain case:

$$F_p = \exp(\Delta \gamma N_p) U_p^{tn} = (I + \Delta \gamma N_p) U_p^{tn} + O(\Delta \gamma^2) \quad (51)$$

It is worth mentioning that the higher-order terms neglected in Eq. (51) could lead to loss of the volume preserving feature of the exponential update and thus spurious volumetric response in the elastic part. However, such deficiency can be neglected with the second assumption of small incremental plastic strain. This will be investigated in the cylindrical necking problem presented in Sect. 6, where the drifting is clearly observed with larger incremental steps.

Finally, when evaluating the algorithmic tangent modulus of the simplified model, the assumptions imply that the contribution of kinematic part \bar{U} can be ignored during iteration thus realising further reduction in computational demand. A more consistent version of the tangent modulus accounting for the nonlinear kinematic relationship is also

Fig. 2 Configurations involved in the simplified hyperelasto-plastic model, with important configurations highlighted with markers



derived for the generalised model as shown in next section. It is noted that similar simplifications of approximating the consistent kinematic measures in the rotated configuration with the ones defined in the intermediate configuration were briefly mentioned in [36, 40]; however, the conditions for viability of the ‘small elastic strain’ assumption and the extent of improvement in efficiency were not addressed. It is

also worth mentioning that the simplified model is not variationally consistent, rather it takes advantage of numerical approximation for simpler code implementation. The overall algorithm is presented below for a particular iteration of global discrete equilibrium along with the proposed simplifications indicated using an asterisk (*).

Algorithm 1: Finite strain hyperelasto-plastic model with logarithmic strains

1. Input Green strains at current iteration, $\mathbf{E}^{t_{n+1}}$, and internal variables from previous step, $\{\mathbf{U}_p^{t_n}, \mathbf{e}_p^{t_n}, \bar{\boldsymbol{\tau}}_B^{t_n}\}$; all non-scalar variables are stored in Voigt form for input and then converted to tensor form.
 2. Compute trial elastic Cauchy deformation tensor according to Eq. (37): $\mathbf{C}_e^{\text{trial}} = (\mathbf{U}_p^{t_n})^{-1} (2\mathbf{E}^{t_{n+1}} + \mathbf{I}) (\mathbf{U}_p^{t_n})^{-1}$.
 3. Compute principal values and directions of $\bar{\mathbf{E}}_e^{\text{trial}}$ and $\mathbf{U}_e^{\text{trial}}$ via spectral decomposition of $\mathbf{C}_e^{\text{trial}}$.
**Compute total trial elastic Green strain $\mathbf{E}_e^{\text{trial}} = \frac{1}{2} (\mathbf{C}_e^{\text{trial}} - \mathbf{I})$.*
 4. Determine the trial rotated Kirchhoff stresses $\bar{\boldsymbol{\tau}}^{\text{trial}}$ based on Hencky’s model formulated in terms of principal logarithmic strains Eq. (25).
**Determine the trial elastic second Piola-Kirchhoff stresses $\mathbf{S}_e^{\text{trial}}$ based on Hencky’s model formulated in terms of total elastic Green strains Eq. (49).*
 5. Input trial stresses into the radial return mapping algorithm and calculate the updated stresses $\bar{\boldsymbol{\tau}}^{t_{n+1}} / \mathbf{S}_e^{t_{n+1}}$ and internal variables $\{\mathbf{e}_p^{t_{n+1}}, \bar{\boldsymbol{\tau}}_B^*\}$
 6. Pull $\bar{\boldsymbol{\tau}}^{t_{n+1}}$ back to reference configuration via Eq. (47).
**Pull $\mathbf{S}_e^{t_{n+1}}$ back to reference configuration via Eq. (50).*
 7. Update the plastic deformation gradient tensor $\mathbf{F}_p^{t_{n+1}}$ according to Eq. (40) and retain its stretch part $\mathbf{U}_p^{t_{n+1}}$ by polar decomposition.
**Update the plastic deformation gradient tensor $\mathbf{F}_p^{t_{n+1}}$ additively according to Eq. (51) and retain its stretch part $\mathbf{U}_p^{t_{n+1}}$ by polar decomposition*
 8. Rotate the back stresses by $\mathbf{R}_p^{t_{n+1}}$, $\bar{\boldsymbol{\tau}}_B^{t_{n+1}} = (\mathbf{R}_p^{t_{n+1}})^T \bar{\boldsymbol{\tau}}_B^* \mathbf{R}_p^{t_{n+1}}$
 9. Determine consistent material tangent modulus \mathbf{D}^{PK2} corresponding to kinematic assumption adopted, stored in a reduced second-order tensor form.
 10. At convergence to global equilibrium, update the internal variables to $\{\mathbf{U}_p^{t_{n+1}}, \mathbf{e}_p^{t_{n+1}}, \bar{\boldsymbol{\tau}}_B^{t_{n+1}}\}$ and set $n \rightarrow n + 1$.
-

5 Consistent tangent modulus in reduced form

An algorithmically consistent tangent modulus is essential for achieving a quadratic rate of convergence in the standard Newton–Raphson iterative procedure [18]. Regarding the algorithm presented above, the complexity of formulating the stiffness tensor mainly arises from the requirement to account for the tangential relationship of deformation measures defined in different configurations. In [9], a highly complex fourth-order tensor form was derived for both the total Lagrangian and updated Lagrangian frameworks, while in [41] numerical perturbation methods based on forward differences were proposed to deal with tangential relationship due to nonlinear kinematic mapping. In this work, it is demonstrated that the consistent tangent modulus could be directly computed and stored in the reduced form which is easier to implement, particularly when internal variables are stored in Voigt form. The proposed derivation follows multiple stages of consecutive transformation between configurations. As indicated in [9], the final fourth-order tensor form only fulfils minor symmetry but not major symmetry; thus, the resulting matrix is slightly asymmetric. In the presentation below, the matrix and vector representations are distinguished from the tensor form by surrounding brackets. $[\bullet]$ represents matrices while $\{\bullet\}$ represents column vectors. The fourth-order tensor is denoted using double struck variables.

Firstly, consider the consistent tangent stiffness associated with full model. The derivation starts with the equivalent expression in the fourth-order tensor form \mathbb{D}^{PK2} , where the reduced form on right-hand side is the desired form:

$$\dot{\mathbf{S}} = \mathbb{D}^{PK2} : \dot{\mathbf{E}} \Leftrightarrow \{\dot{\mathbf{S}}\} = [\mathbb{D}^{PK2}] \{\dot{\mathbf{E}}\} \tag{52}$$

Eq. (52) is pushed to the trial intermediate configuration by the plastic deformation gradient tensor from previous step considering Eq. (47):

$$\dot{\mathbf{S}}_e^{trial} = \mathbb{D}^{EPK2} : \dot{\mathbf{E}}_e^{trial} \Leftrightarrow \{\dot{\mathbf{S}}_e^{trial}\} = [\mathbb{D}^{EPK2}] \{\dot{\mathbf{E}}_e^{trial}\} \tag{53}$$

noting that the stresses and strains in this equation should be trial values. The tangent stiffness \mathbb{D}^{EPK2} relates the elastic second Piola–Kirchhoff stress rates to the elastic Green strain rates. Its indexed form can be obtained as the result of push forward operation on \mathbb{D}^{PK2} and vice versa. To avoid confusion when we consider multiple stages during derivation, the index set $\{a, b, c, d\}$ always describes the configuration before push forward/pull backwards, whereas set $\{i, j, k, l\}$ describes that after transformation. For example, they describe the intermediate and reference configuration, respectively, in current stage for the equation below:

$$\mathbb{D}_{ijkl}^{PK2} = \left(\mathbf{U}_p^{tn}\right)_{ia}^{-1} \left(\mathbf{U}_p^{tn}\right)_{jb}^{-1} \left(\mathbf{U}_p^{tn}\right)_{kc}^{-1} \left(\mathbf{U}_p^{tn}\right)_{ld}^{-1} \mathbb{D}_{abcd}^{EPK2} \tag{54}$$

The numerical implementation of Eq. (54) is slightly cumbersome and unsuitable for our framework. In an alternative matrix representation, the tensor mapping is replaced by an equivalent matrix:

$$\dot{\mathbf{S}} = \left(\mathbf{U}_p^{tn}\right)^{-1} \dot{\mathbf{S}}_e^{trial} \left(\mathbf{U}_p^{tn}\right)^{-1} \Leftrightarrow \{\dot{\mathbf{S}}\} = [\mathbf{T}^{EPK2}] \{\dot{\mathbf{S}}_e^{trial}\} \tag{55}$$

For any configuration transformation operations with general form $\mathbf{Z}' = \mathbf{Y}\mathbf{Z}\mathbf{Y}^T$, where \mathbf{Y} is a proper kinematic tensor and \mathbf{Z} is an arbitrary symmetric tensor, the transformation matrix can be derived from its index format:

$$Z'_{ij} = Y_{ia} Z_{ab} Y_{jb} \tag{56}$$

The components of the general transformation matrix $[\mathbf{T}^Z]$ for $\{\mathbf{Z}'\} = [\mathbf{T}^Z] \{\mathbf{Z}\}$ then follow as below provided the Voigt form of \mathbf{Z} is the same as that for stresses, i.e. without coefficient of 2 for shear components:

$$[\mathbf{T}^Z] = \begin{bmatrix} \mathbf{T}_{11}^Z & \mathbf{T}_{12}^Z \\ \mathbf{T}_{21}^Z & \mathbf{T}_{22}^Z \end{bmatrix} \tag{57a}$$

where

$$[\mathbf{T}_{11}^Z] = \begin{bmatrix} Y_{11}^2 & Y_{12}^2 & Y_{13}^2 \\ Y_{21}^2 & Y_{22}^2 & Y_{23}^2 \\ Y_{31}^2 & Y_{32}^2 & Y_{33}^2 \end{bmatrix} \tag{57b}$$

$$[\mathbf{T}_{12}^Z] = \begin{bmatrix} 2Y_{12}Y_{13} & 2Y_{11}Y_{13} & 2Y_{11}Y_{12} \\ 2Y_{22}Y_{23} & 2Y_{21}Y_{23} & 2Y_{21}Y_{22} \\ 2Y_{32}Y_{33} & 2Y_{31}Y_{33} & 2Y_{31}Y_{32} \end{bmatrix} \tag{57c}$$

$$[\mathbf{T}_{21}^Z] = \begin{bmatrix} Y_{21}Y_{31} & Y_{22}Y_{32} & Y_{23}Y_{33} \\ Y_{11}Y_{31} & Y_{12}Y_{32} & Y_{13}Y_{33} \\ Y_{11}Y_{21} & Y_{12}Y_{22} & Y_{13}Y_{23} \end{bmatrix} \tag{57d}$$

$$[\mathbf{T}_{22}^Z] = \begin{bmatrix} Y_{22}Y_{33} + Y_{23}Y_{32} & Y_{21}Y_{33} + Y_{23}Y_{31} & Y_{21}Y_{32} + Y_{22}Y_{31} \\ Y_{12}Y_{33} + Y_{13}Y_{32} & Y_{11}Y_{33} + Y_{13}Y_{31} & Y_{11}Y_{32} + Y_{12}Y_{31} \\ Y_{12}Y_{23} + Y_{13}Y_{22} & Y_{11}Y_{23} + Y_{13}Y_{21} & Y_{11}Y_{22} + Y_{12}Y_{21} \end{bmatrix} \tag{57e}$$

Concerning Eq. (55), $[\mathbf{T}^{EPK2}]$ then takes the form of Eq. (57) with $\mathbf{Y} = \left(\mathbf{U}_p^{tn}\right)^{-1}$. On the other hand, the corresponding work conjugate strain should undergo the linear mapping described by $[\mathbf{T}^{EPK2}]^{-T}$, as can be shown from the virtual power balance between different conjugate pairs. In [9], the tangential relationship between strain rates is achieved instead in the eigenspace first and then converted back using the rotation tensor containing principal directions, which is more complicated and significantly more computationally demanding. Assuming that the reduced

form of $[D^{EPK2}]$ is known, the substitution of Eq. (55) and the strain transformation into Eq. (52) yield $[D^{PK2}]$ as:

$$[D^{PK2}] = [T^{EPK2}] [D^{EPK2}] [T^{EPK2}]^T \tag{58}$$

Next following the same reasoning, pushing Eq. (53) forward to the rotated configuration where the radial return mapping is performed leads to:

$$\dot{\bar{\tau}} = \mathbb{D}^{RK} : \dot{\bar{E}}_e \Leftrightarrow \left\{ \frac{\dot{\bar{\tau}}}{\bar{\tau}} \right\} = [D^{RK}] \left\{ \frac{\dot{\bar{E}}_e}{\bar{E}_e} \right\} \tag{59}$$

Note that at this stage, transformation of stress rates requires also inclusion of the contribution from the change of kinematic quantities by the chain rule, whereas for the previous stage the kinematic quantity used for pulling backwards is the previous plastic deformation gradient and hence is stationary:

$$\begin{aligned} \dot{S}_e^{trial} &\approx (U_e^{trial})^{-1} \dot{\bar{\tau}} (U_e^{trial})^{-1} \\ &= (U_e^{trial})^{-1} \dot{\bar{\tau}} (U_e^{trial})^{-1} + (U_e^{trial})^{-1} \dot{\bar{\tau}} (U_e^{trial})^{-1} + (U_e^{trial})^{-1} \dot{\bar{\tau}} (U_e^{trial})^{-1} \\ &= -(U_e^{trial})^{-1} \cdot \dot{U}_e^{trial} \cdot S_e + (U_e^{trial})^{-1} \dot{\bar{\tau}} (U_e^{trial})^{-1} - S_e \cdot \dot{U}_e^{trial} \cdot (U_e^{trial})^{-1} \end{aligned} \tag{60}$$

The terms in the last equation should be treated separately. The middle term accounts for rate of change of rotated Kirchhoff stresses pulled backwards to the intermediate configuration whereas the two other terms are attributed to the rate of change of trial elastic strains. The former is determined by the same procedure as in the previous stage, except that now the stress transformation matrix $[T^{RK}]$ is composed of entries from the inverse of trial elastic stretches. The symmetric tangent stiffness from the return mapping algorithm $[D^{RK}]$ has the same form as the classical infinitesimal strain case. In analogy with Eq. (58), the overall contribution from this term to $[D^{EPK2}]$ would be $[T^{RK}] [D^{RK}] [T^{RK}]^T$.

Other terms concerning the rate of change of the trial elastic stretch with respect to the elastic Green strain rate require additional effort in deriving the matrix form. Instead of examining their relationship in the eigenspace, its inverse form is directly evaluated:

$$\dot{E}_e^{trial} = T^E : \dot{U}_e^{trial} \Leftrightarrow \left\{ \dot{E}_e^{trial} \right\} = [T^E] \left\{ \dot{U}_e^{trial} \right\} \tag{61}$$

It is worth mentioning the Voigt form for stretch tensor follows the same structure as stress tensor, i.e. no factor of 2

applied to the non-axial stretch components. The reason for such arrangement will be explained later.

The transformation matrix $[T^E]$ can again be derived from the indexed form of the trial elastic Green strain definition.

$$(E_e^{trial})_{ij} = \frac{1}{2} \left[(U_e^{trial})_{ia} (U_e^{trial})_{jb} - \delta_{ij} \right] \tag{62}$$

where δ_{ij} is the Kronecker delta. A specific element in the matrix is computed by expanding the index form and evaluating derivatives against the corresponding components of the stretch tensor. For a concise presentation, U_e^{trial} is replaced by G only in the following:

$$[T^E] = \begin{bmatrix} T_{11}^E & T_{12}^E \\ T_{21}^E & T_{22}^E \end{bmatrix} \tag{63a}$$

where

$$[T_{11}^E] = \begin{bmatrix} G_{11} & 0 & 0 \\ 0 & G_{22} & 0 \\ 0 & 0 & G_{33} \end{bmatrix} \tag{63b}$$

$$[T_{12}^E] = [T_{21}^E]^T = \begin{bmatrix} 0 & G_{13} & G_{12} \\ G_{23} & 0 & G_{12} \\ G_{23} & G_{13} & 0 \end{bmatrix} \tag{63c}$$

$$[T_{22}^E] = \begin{bmatrix} G_{22} + G_{33} & G_{12} & G_{13} \\ G_{12} & G_{11} + G_{33} & G_{23} \\ G_{13} & G_{23} & G_{11} + G_{22} \end{bmatrix} \tag{63d}$$

Subsequently, according to Eq. (60), the trial elastic stretch rate is multiplied by additional elastic second Piola–Kirchhoff stresses and inverse of the trial elastic stretch at the current step. By exploiting the arrangement of Voigt form of stretch tensor, mapping due to those additional terms could be gathered into a single matrix $[T^{E2}]$ with a similar form as Eq. (57) according to Eq. (56). The Y matrix would be both S_e and $(U_e^{trial})^{-1}$ depending on their position in the expression. To sum up all parts in Eq. (60):

$$[D^{EPK2}] = [TRK][DRK][TRK]^T - [TE2][TE]^{-1} \tag{64}$$

The first contribution stemming from the return mapping tangent stiffness normally outweighs the other. Also, asymmetry of the matrix results from the second term in Eq. (64), although due to difference in magnitude, its extent is minor. However, for a rigorous satisfaction of quadratic rate of convergence, neither of them should be discarded. By Eq. (58), the final consistent stiffness matrix for the total Lagrangian framework would be:

$$[DPK2] = [TEPK2] \left\{ [TRK][DRK][TRK]^T - [TE2][TE]^{-1} \right\} [TEPK2]^T \tag{65}$$

For the simplified model, as the rotated Kirchhoff stresses is no longer involved in the computation, the evaluation of the tangent stiffness is simplified significantly. Only the first stage in our previous analysis is concerned. This is effectively because under the model assumptions, the trial elastic deformation would hardly vary with small increment step size, thus the contribution from that part in Eq. (60) can be neglected. In this case the consistent tangent stiffness adopts a similar form as Eq. (58), noting its symmetric property:

$$[D_{Sim}^{PK2}] = [TEPK2] [D_{sim}^{EPK2}] [TEPK2]^T \tag{66}$$

The simplified matrix $[D_{sim}^{EPK2}]$ has exactly the same formulation as $[DRK]$ being consistent with the radial return mapping algorithm.

6 Numerical examples

The full and simplified hyperelasto-plasticity models have been implemented in the nonlinear finite element analysis program ADAPTIC [42]. This section assesses performance of the models against two benchmark numerical examples in the literature by focusing on accuracy and efficiency of the simplified model.

(a) Taylor bar impact problem

The first numerical problem simulates impact of a cylindrical bar onto a rigid frictionless plate at a high

speed of 227 m/s via explicit or implicit dynamic time-integration schemes [39]. The experimental setup was initially proposed by Taylor [43] to investigate viscoplastic behaviour of metals under very high loading rate. A standard finite element model configuration was initially considered in [8] and subsequently also analysed in [9, 44], where the rate-independent plasticity model was employed.

The sample bar has a radius of 3.2 mm and a length of 32.4 mm, and the von Mises yield criterion with linear hardening is employed. All relevant material parameters shown in Table 1 are consistent with past literature. The time interval of interest is 80 μs from the point where the bar comes into contact with the rigid plate, which is modelled here by imposing restraints on base of the bar. Due to symmetry of the problem, only a quarter of the bar is modelled with 912 20-noded quadratic brick continuum elements. It is well known that the pure displacement based linear elements are susceptible to volumetric locking for near incompressible or fully incompressible material, as the low-order elements fail to represent the actual volume-preserving motion. In this study, we circumvented the issue by adopting higher-order elements with reduced integration. Other solutions based on assumed strain elements [45], F-bar method [46], and hybrid element formulations may also be considered. The mesh is refined near the base where the most significant and localised plastic deformation takes place. A full model is also con-

Table 1 Material parameters for Taylor bar impact problem

Material parameters	Values [units]
Young’s modulus, E	1.17×10^5 [MPa]
Poisson ratio, ν	0.35 [-]
Initial yield stress, σ_{Y0}	400 [MPa]
Hardening modulus, H	100 [MPa]
Density in undeformed state, ρ_0	8930 [kg/m ³]

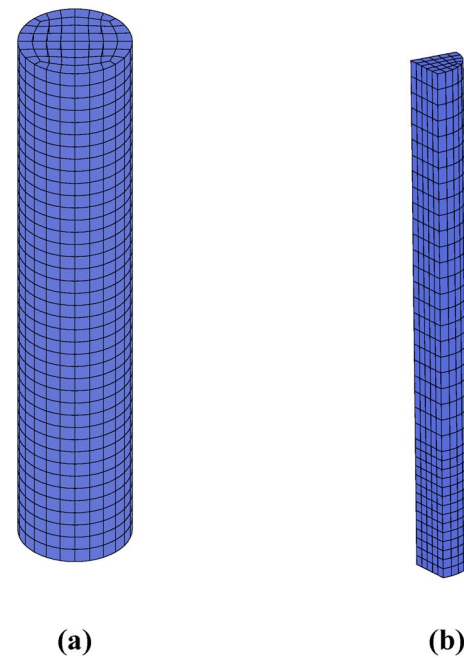


Fig. 3 Mesh for **a** full model and **b** quarter model

Fig. 4 Mesh configuration at **a** $t = 0\mu\text{s}$; **b** $t = 40\mu\text{s}$; **c** $t = 80\mu\text{s}$; **d** $t = 80\mu\text{s}$ (full model)

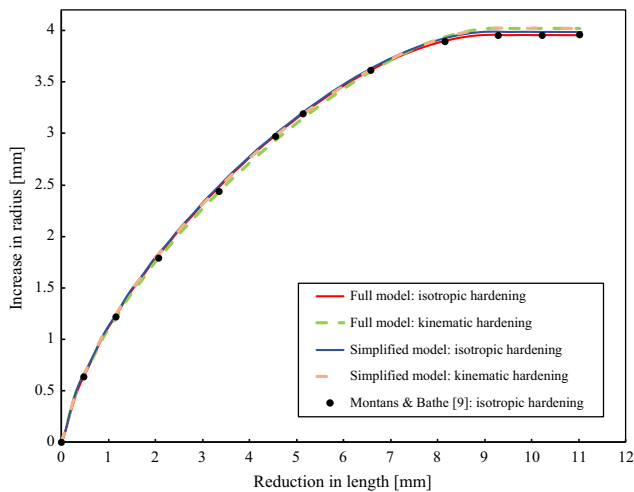
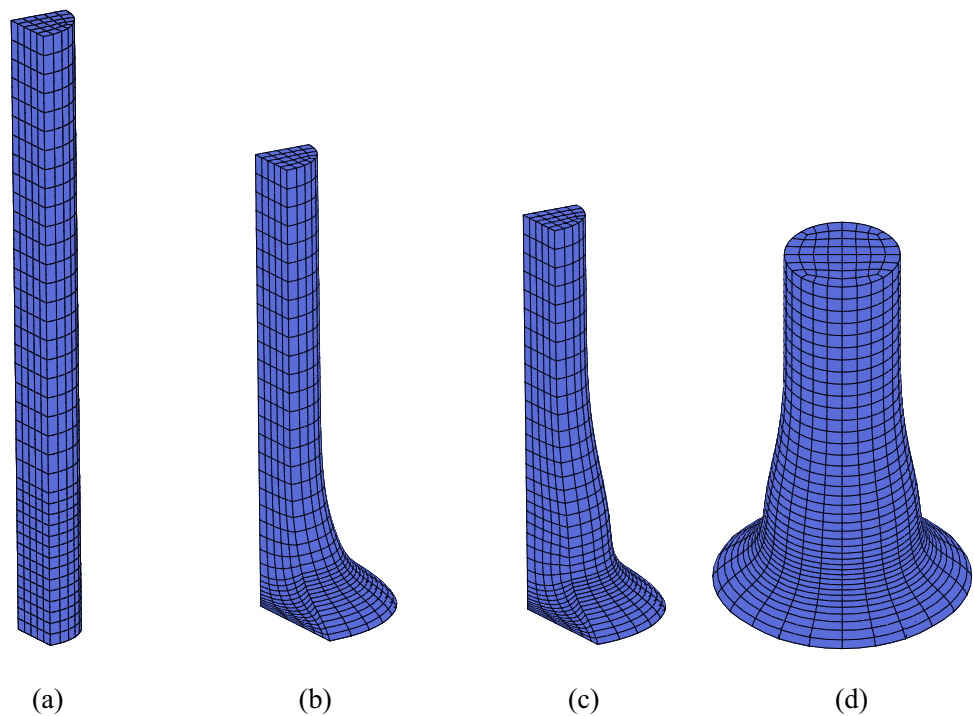


Fig. 5 Radial expansion against axial shortening for different hardening cases using implicit scheme

structured for presenting the overall deformation shape only. Figure 3 shows the mesh for the reduced and the full model, whereas Fig. 4 shows the deformed quarter mesh at $t = 0, 40, 80\mu\text{s}$, respectively.

Figure 5 shows the results of the radial deformation against the axial shortening for cases of different hardening types using the implicit scheme. Both the final enlarged radius and shortened length exhibit a favourable comparison with results reported in the literature. As can be observed from the figure, no significant deviation in the impact response is observed for iso-

Table 2 Final bar geometry for different hardening type, model type and dynamic schemes

Analysis type	Hardening	Model type	Final radius [mm]	Final length [mm]
Implicit	Isotropic	Full	7.152	21.418
	Isotropic	Simplified	7.180	21.350
	Kinematic	Full	7.193	21.371
	Kinematic	Simplified	7.222	21.302
Explicit	Isotropic	Full	6.949	21.586
	Isotropic	Simplified	6.944	21.527
	Kinematic	Full	7.134	21.519
	Kinematic	Simplified	7.137	21.458

Table 3 Comparison of CPU time for implicit and explicit dynamic schemes

Analysis type	Model type	Number of steps	Average CPU time per step [s]	Factor
Implicit	Full	10,000	1.159	1.15
	Simplified	10,000	1.009	
Explicit	Full	280,000	0.097	1.83
	Simplified	280,000	0.053	

tropic and kinematic hardening. In addition, it is shown that the simplified model can achieve the same level of accuracy as the full model. For both the isotropic and kinematic hardening cases, the final radial deformation

differs by only around 0.7% between the full and simplified models. In general, the simplified model leads to a slightly less stiff response compared to the full model, evidenced by the slightly increased shortening at the end of analysis.

The final radius and length of the bar obtained from both implicit and explicit analyses are provided in Table 2. For the purpose of comparing the computational efficiency of the simplified model, we limit the case to isotropic hardening only and list above the average CPU time per step for the implicit and explicit analysis in Table 3. The limiting size of time step for stability in explicit dynamic scheme depends on the minimum characteristic size of the element. Importantly, for problems where the mesh undergoes significant distortion, the time-step size has to be reduced further with a reducing element size in the deformed configuration. Remedies for this issue involve adaptive remeshing or adopting another framework such as the material point method [47]. However, a small time-step size also renders the second assumption for the simplified model increasingly valid. As evident from Table 3, the simplified model can provide a significant reduction in computing time of around 45% (efficiency factor 1.83) for the explicit analysis and a relatively smaller reduction of around 13% (efficiency factor 1.15) in the implicit analysis. Although the savings in computing time depend also on the actual code implementation, it is evident that the simplified model is significantly more efficient than the full model, without compromising accuracy, by virtue of avoiding expensive algorithmic operations that are not highly relevant to finite strain analysis of metallic structures. Note also that the reduction in computing time in explicit scheme can reflect the constitutive model efficiency to a greater extent than in the implicit scheme, where significant additional effort is devoted in the latter scheme to solving the global system of equilibrium equations. It is also observed that at large strains, normally towards the end of analysis, the simplified model requires slightly less global iterations for convergence than the full model, which may be attributed to the simpler kinematic relationships.

(b) Cylindrical necking problem

The second numerical example involves a cylindrical rod subjected to uniaxial extension to the large deformation range with significant plasticity localised in the necking region. Similar to the previous example, this problem was studied previously by several researchers [8, 9, 14, 15, 18]. A brief summary of variants of numerical model setup can also be found in a recent paper [14]. Again, the von Mises yield crite-

Table 4 Material parameters for the cylindrical necking problem

Material parameters	Values [units]
Young's modulus, E	2.069×10^5 [MPa]
Poisson ratio, ν	0.29 [-]
Initial yield stress, σ_{Y0}	450 [MPa]
Saturation yield stress, $\sigma_{Y\infty}$	715 [MPa]
Hardening modulus, H	130 [MPa]
Saturation parameter, θ	16.93 [-]
Density in undeformed state, ρ_0	8930 [kg/m ³]

rion is adopted, together with a saturation type of yield stresses:

$$\sigma_Y(e_p) = \sigma_{Y0} + R(e_p) = \sigma_{Y0} + (\sigma_{Y\infty} - \sigma_{Y0}) (1 - \exp(-\theta e_p)) + H e_p \quad (67)$$

where $\sigma_{Y\infty}$ is the saturated yield stress; θ is a parameter controlling the rate of saturation; and H is the linear hardening modulus.

In this example, we consider the isotropic hardening only, with the material parameters listed in Table 4, and the model geometry following the setup in [14]. The rod has a radius of 6.413 mm at both ends and a total length of 53.34 mm. To trigger necking as one of the bifurcation paths in uniaxial extension, geometric imperfection is introduced in the form of a linearly reduced radius from the value at ends to 6.35 mm at the central section. Due to the symmetry of the problem, only one-eighth of the rod is meshed, and corresponding boundary conditions are imposed on all faces of the model. At the longitudinal ends of the rod, the boundary condition is simply supported without shear induced in the neighbourhood; thus, in-plane deformation is allowed at the support ends. The reduced model is then subjected to a quasi-static displacement up to 7 mm corresponding to an engineering strain of 26%. The axisymmetric mesh shown in Fig. 6 consists of 152 quadratic 15-noded wedge elements placed around the innermost loop and 1672 20-noded brick elements placed around outer loops over cross section. The mesh near the central section where localised finite strain plasticity expected is refined. Figure 7 shows the deformed mesh configuration at $u = 0, 2.3, 4.6, 7$ mm, respectively.

The force–displacement response is shown in Fig. 8 for the whole bar, whereas Fig. 9 presents the variation in the necking radius with the longitudinal displacement. The final radius obtained from the full model is 2.64 mm, which compares well with the result obtained

Fig. 6 Reduced axisymmetric mesh for the cylindrical rod

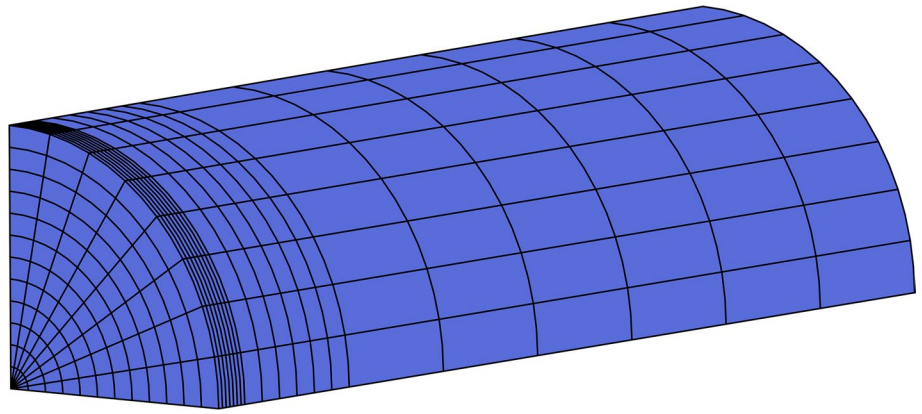
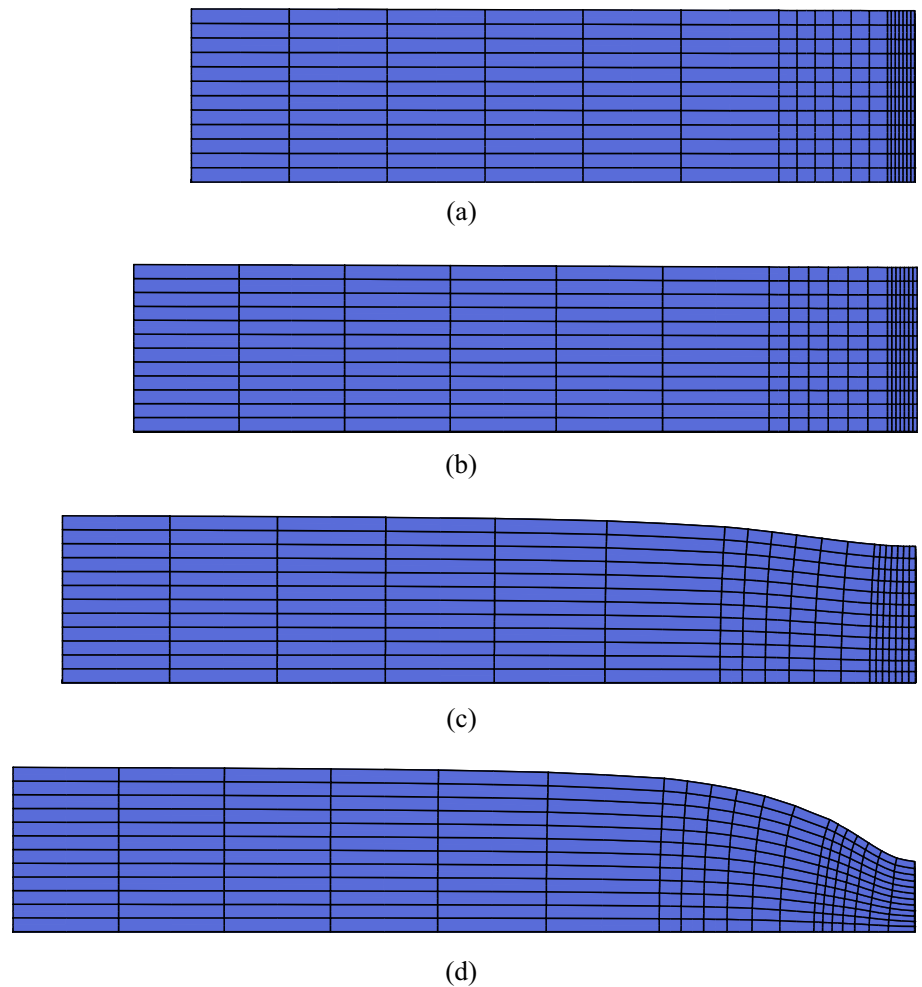


Fig. 7 Mesh configuration at **a** $u = 0\text{mm}$; **b** $u = 2.3\text{mm}$; **c** $u = 4.6\text{mm}$; **d** $u = 7\text{mm}$



in [14]. However, the result obtained from simplified model with the same number of steps drifts from the full model results in the softening range, and it can be observed that the deviation vanishes with a smaller step size. With a tenfold increase in the number of steps, the necking radius obtained from the simplified model differs by around 8% from that obtained from the full

model with 100 steps. In addition, from Fig. 8, the simplified model tends to provide a stiffer response, with the deviation gradually increasing in the softening post-necking range. This is attributed to the stricter assumptions on incremental strains and trial elastic strains in the simplified model compared to the full model. This transition in relative accuracy approximately corresponds to

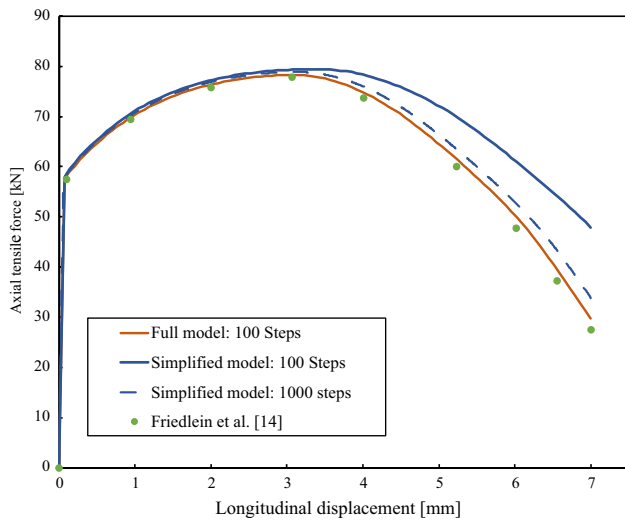


Fig. 8 Force–displacement response for the whole bar

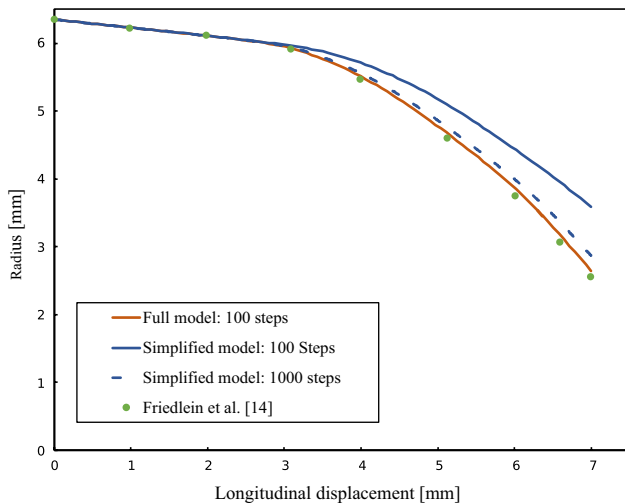


Fig. 9 Necking radius against axial displacements for different model types and step size

the start of necking, as also indicated by an accelerating rate of radial reduction. This may be explained by the fact that after necking is initiated, deformation becomes non-homogeneous and the strain increments between steps become much more significant near the middle section compared to the homogeneous case. Accordingly, for material points in necking region, the elastic Green strains can no longer approximate the logarithmic strains by neglecting the higher order terms in Taylor expansions. Actually, for tensile stretch greater than 1, these additional terms lead to lower logarithmic strain than the elastic Green strains. This in turn gives lower predicted stresses from the return mapping algorithm which may even decrease due to the pull backwards operation Eq. (47). Note the situation is reversed if the deformation is compressive; as observed in the previous example, the simplified model gives a less stiff response for compressive deformation.

To fully establish the factors responsible for drifting, simplifications of kinematic quantities, as given by Eqs. (48) and (50), and the exponential update, as given by Eq. (51), are investigated separately with 50 and 100 incremental steps. The results presented in Fig. 10 are obtained from three models: (1) full model; (2) full model with linearised exponential mapping only; and (3) model with simplified kinematic relationship and the original exponential mapping, respectively. Thus, the plastic flow in Model 2 takes place in the logarithmic space with the linearised update of Eq. (51), whereas in Model 3 it takes place in the trial intermediate configuration with the simplifications of Eqs. (48) and (50) while using the full exponential update.

Although in principle the linearised exponential mapping can potentially cause drifting that becomes worse with a larger step size, the results in Fig. 10 show that even with a relatively large step size at 50 incremental steps, the associated drifting (Model 2) is

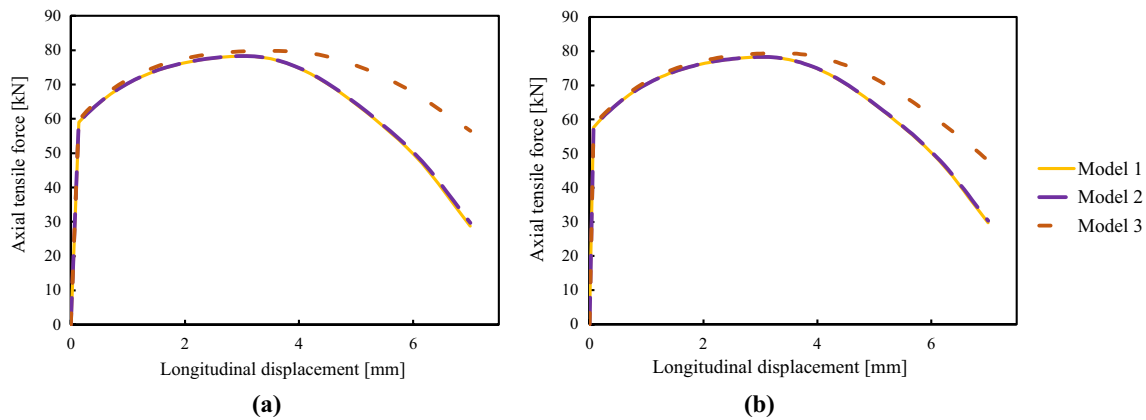


Fig. 10 Force–displacement of cylindrical necking problem with different time step size. **a** 50 steps; **b** 100 steps

considerably small compared to the deviation caused by the simplified kinematic transformation and plastic flow in the Green strain space (Model 3). Importantly, the error associated with the latter also reduces with step size, as can be seen from comparing the results in Fig. 10a, b, with good accuracy achieved at 1000 steps as shown in the previous results of Fig. 8. For typical explicit dynamic analysis or other analysis requiring small time steps, e.g. ductile fracture modelling, the overall deviation has been shown to be negligible while achieving significant computational savings.

7 Conclusions

This work presents a finite strain hyperelasto-plastic material model formulated in a total Lagrangian framework, where significant simplifications are proposed for ease of implementation and computational efficiency, while maintaining applicability to the large deformation analysis of 3D continuum metallic structures.

The main simplifications proposed relate to the geometric transformation processes, avoiding the need for spectral/polar decomposition and expensive exponential/logarithmic functions. In addition, the consistent tangent stiffness is derived in a reduced second-order form for both the full and simplified models. Besides the realised computational efficiency, the proposed modifications allow a more concise and straightforward code implementation particularly when stresses and strains are stored in Voigt form. Furthermore, the simplified model resembles the infinitesimal strain elasto-plasticity model with the additive update rule.

Two numerical examples are presented to verify the accuracy and efficiency of the proposed simplified model. We show in the first example that for problems where a relatively small time-step size is required; for example, in explicit dynamic analysis for impact problems, the simplifications can lead to a reduction in computational demand by almost 50%. In the second example, the limitation of the simplified model is demonstrated in terms of the required step size, where convergence to the full model results is achieved with a sufficiently small step.

Finally, although this work has considered the von Mises yield function with a single back stress measure, the proposed model can be extended to include more general and complex plasticity features since the kinematic simplifications focuses on the geometric transformations between different strain/stress measures rather than the underlying treatment of material plasticity.

Acknowledgements Authors gratefully acknowledge the funding provided by the Chinese Scholarship Council under grant 202008060195 for supporting doctoral study of the first author.

Data availability Data generated during this study are available from the corresponding author upon reasonable request.

Declarations

Conflict of interest The authors have no competing interests to declare that are relevant to the content of this article.

Open Access This article is licensed under a Creative Commons Attribution 4.0 International License, which permits use, sharing, adaptation, distribution and reproduction in any medium or format, as long as you give appropriate credit to the original author(s) and the source, provide a link to the Creative Commons licence, and indicate if changes were made. The images or other third party material in this article are included in the article's Creative Commons licence, unless indicated otherwise in a credit line to the material. If material is not included in the article's Creative Commons licence and your intended use is not permitted by statutory regulation or exceeds the permitted use, you will need to obtain permission directly from the copyright holder. To view a copy of this licence, visit <http://creativecommons.org/licenses/by/4.0/>.

References

1. Xiao H, Bruhns OT, Meyers A (2005) Elastoplasticity beyond small deformations. *Acta Mech* 63:18–48. <https://doi.org/10.1007/s00707-005-0282-7>
2. Pinsky PM, Ortiz M, Pister KS (1983) Numerical integration of rate constitutive equations in finite deformation analysis. *Comput Methods Appl Mech Eng* 40:137–158. [https://doi.org/10.1016/0045-7825\(83\)90087-7](https://doi.org/10.1016/0045-7825(83)90087-7)
3. Xiao H, Bruhns OT, Meyers A (1997) A hypo-elasticity model based upon the logarithmic stress rate. *J Elast* 47:51–68. <https://doi.org/10.1023/A:1007356925912>
4. Bruhns OT, Xiao H, Meyers A (2005) A weakened form of Ilyushin's postulate and the structure of self-consistent Eulerian finite elastoplasticity. *Int J Plast* 21:199–219. <https://doi.org/10.1016/j.ijplas.2003.11.015>
5. Zhu Y, Kang G, Kan Q, Bruhns OT (2014) Logarithmic stress rate based constitutive model for cyclic loading in finite plasticity. *Int J Plast* 54:34–55. <https://doi.org/10.1016/j.ijplas.2013.08.004>
6. Eterovic AL, Bathe KJ (1990) A hyperelastic-based large strain elasto-plastic constitutive formulation with combined isotropic-kinematic hardening using the logarithmic stress and strain measures. *Int J Numer Meth Eng* 30:1099–1114. <https://doi.org/10.1002/nme.1620300602>
7. Weber G, Anand L (1990) Finite deformation constitutive equations and a time integration procedure for isotropic, hyperelastic-viscoplastic solids. *Comput Methods Appl Mech Eng* 79:173–202. [https://doi.org/10.1016/0045-7825\(90\)90131-5](https://doi.org/10.1016/0045-7825(90)90131-5)
8. Simo JC (1992) Algorithms for static and dynamic multiplicative plasticity that preserve the classical return mapping schemes of the infinitesimal theory. *Comput Methods Appl Mech Eng* 99(1):61–112. [https://doi.org/10.1016/0045-7825\(92\)90123-2](https://doi.org/10.1016/0045-7825(92)90123-2)
9. Montáns FJ, Bathe KJ (2005) Computational issues in large strain elasto-plasticity: an algorithm for mixed hardening and plastic spin. *Int J Numer Meth Eng* 63:159–196. <https://doi.org/10.1002/nme.1270>
10. Caminero MA, Montáns FJ, Bathe KJ (2011) Modelling large strain anisotropic elasto-plasticity with logarithmic strain and stress measures. *Comput Struct* 89(11–12):826–843. <https://doi.org/10.1016/j.compstruc.2011.02.011>
11. Nguyen K, Sanz MA, Montáns FJ (2020) Plane-stress constrained multiplicative hyperelasto-plasticity with nonlinear kinematic

- hardening. Consistent theory based on elastic corrector rates and algorithmic implementation. *Int J Plast*. <https://doi.org/10.1016/j.ijplas.2019.08.017>
12. Green AE, Naghdi PM (1965) A general theory of an elastic–plastic continuum. *Arch Rational Mech Anal* 18:251–281. <https://doi.org/10.1007/BF00251666>
 13. Miehe C, Apel N, Lambrecht M (2002) Anisotropic additive plasticity in the logarithmic strain space: modular kinematic formulation and implementation based on incremental minimisation principles for standard materials. *Comput Methods Appl Mech Eng* 191:5383–5425. [https://doi.org/10.1016/S0045-7825\(02\)00438-3](https://doi.org/10.1016/S0045-7825(02)00438-3)
 14. Friedlein J, Mergheim J, Steinmann P (2022) Observations on additive plasticity in the logarithmic strain space at excessive strains. *Int J Solids Struct* 239–240:111416. <https://doi.org/10.1016/j.ijsolstr.2021.111416>
 15. Miehe C (1998) A formulation of finite elastoplasticity based on dual co- and contra-variant eigenvector triads normalized with respect to a plastic metric. *Comput Methods Appl Mech Eng* 159:223–260. [https://doi.org/10.1016/S0045-7825\(97\)00273-9](https://doi.org/10.1016/S0045-7825(97)00273-9)
 16. Miehe C (1998) A constitutive frame of elastoplasticity at large strains based on the notion of a plastic metric. *Int J Solids Struct* 35:3859–3897. [https://doi.org/10.1016/S0020-7683\(97\)00175-3](https://doi.org/10.1016/S0020-7683(97)00175-3)
 17. Bruhns OT (2020) Large deformation plasticity. *Acta Mech Sin* 36:472–492. <https://doi.org/10.1007/s10409-020-00926-7>
 18. Simo JC, Hughes TJR (1998) *Computational inelasticity*. Springer, New York, NY
 19. Brepols T, Vladimirov IN, Reese S (2014) Numerical comparison of isotropic hypo- and hyperelastic-based plasticity models with applications to industrial forming processes. *Int J Plast* 63:18–48. <https://doi.org/10.1016/j.ijplas.2014.06.003>
 20. Meyers A, Schießle P, Bruhns OT (2000) Some comments on objective rates of symmetric Eulerian tensors with application to Eulerian strain rates. *Acta Mech* 139:91–103. <https://doi.org/10.1007/BF01170184>
 21. Xiao H, Bruhns OT, Meyers A (1997) On objective corotational rates and their defining spin tensors. *Int J Solids Struct* 35:4001–4014. [https://doi.org/10.1016/S0020-7683\(97\)00267-9](https://doi.org/10.1016/S0020-7683(97)00267-9)
 22. Prager W (1960) An elementary discussion of definitions of stress rate. *Quart Appl Math* 18:403–407
 23. Nagtegaal JC, de Jong JE (1982) Some aspects of non-isotropic work hardening in finite strain plasticity. *Plasticity of metals at finite strain, theory, computation and experiment*. Stanford University, Stanford, pp 65–106
 24. Dienes JK (1979) On the analysis of rotation and stress rate in deforming bodies. *Acta Mech* 32:217–232. <https://doi.org/10.1007/BF01379008>
 25. Simo JC, Pister KS (1984) Remarks on rate constitutive equations for finite deformation problems: computational implications. *Comput Methods Appl Mech Eng* 46:201–215. [https://doi.org/10.1016/0045-7825\(84\)90062-8](https://doi.org/10.1016/0045-7825(84)90062-8)
 26. Shutov AV, Ihlemann J (2014) Analysis of some basic approaches to finite strain elasto-plasticity in view of reference change. *Int J Plast* 63:183–197. <https://doi.org/10.1016/j.ijplas.2014.07.004>
 27. Zhang M, Montáns FJ (2019) A simple formulation for large-strain cyclic hyperelasto-plasticity using elastic correctors. Theory and algorithmic implementation. *Int J Plast* 113:185–217. <https://doi.org/10.1016/j.ijplas.2018.09.013>
 28. Lee EH (1969) Elastic-plastic deformation at finite strains. *J Appl Mech* 36:1–6. <https://doi.org/10.1115/1.3564580>
 29. Hughes TJR, Winget J (1980) Finite rotation effects in numerical integration of rate constitutive equations arising in large-deformation analysis. *Int J Numer Meth Eng* 15:1862–1867. <https://doi.org/10.1002/nme.1620151210>
 30. Simo JC (1988) A framework for finite strain elastoplasticity based on maximum plastic dissipation and the multiplicative decomposition: part I. Continuum formulation. *Comput Methods Appl Mech Eng* 66:199–219. [https://doi.org/10.1016/0045-7825\(88\)90076-X](https://doi.org/10.1016/0045-7825(88)90076-X)
 31. Simo JC (1988) A framework for finite strain elastoplasticity based on maximum plastic dissipation and the multiplicative decomposition: part II. Computational aspects. *Comput Methods Appl Mech Eng* 68:1–31. [https://doi.org/10.1016/0045-7825\(88\)90104-1](https://doi.org/10.1016/0045-7825(88)90104-1)
 32. Simo JC, Meschke G (1993) A new class of algorithms for classical plasticity extended to finite strains. *Comput Mech* 11:253–278. <https://doi.org/10.1007/BF00371865>
 33. Itskov M (2004) On the application of additive decomposition of generalised strain measures in large strain plasticity. *Mech Res Commun* 31:507–517. <https://doi.org/10.1016/j.mechrescom.2004.02.006>
 34. Papadopoulos P, Lu J (1998) A general framework for the numerical solution of problems in finite elasto-plasticity. *Comput Methods Appl Mech Eng* 159:1–18. [https://doi.org/10.1016/S0045-7825\(98\)80101-1](https://doi.org/10.1016/S0045-7825(98)80101-1)
 35. Neff P, Ghiba ID (2016) Loss of ellipticity for non-coaxial plastic deformations in additive logarithmic finite strain plasticity. *Int J Non-linear Mech* 81:122–128. <https://doi.org/10.1016/j.ijnonlinmec.2016.01.003>
 36. Gurtin ME, Fried E, Anand L (2013) *The mechanics and thermodynamics of continua*. Cambridge University Press, Cambridge
 37. Lee EH (1981) A correct definition of elastic and plastic deformation and its computational significance. *J Appl Mech* 48:35–40. <https://doi.org/10.1115/1.3157589>
 38. Plešek J, Krusová A (2006) Formulation, validation and numerical procedures for Hencky’s elasticity model. *Comput Struct* 84:1141–1150. <https://doi.org/10.1016/j.compstruc.2006.01.005>
 39. Sautter KB, Meßmer M, Teschemacher T, Bletzinger K (2022) Limitations of the St. Venant-Kirchhoff material model in large strain regimes. *Int J Non Linear Mech* 147:104207. <https://doi.org/10.1016/j.ijnonlinmec.2022.104207>
 40. Belytschko T, Liu WK, Moran B, Elkhodary K (2014) *Nonlinear finite elements for continua and structures*. John Wiley & sons, New Jersey
 41. Miehe C (1996) Numerical computation of algorithmic (consistent) tangent moduli in large-strain computational inelasticity. *Comput Methods Appl Mech Eng* 134:223–240. [https://doi.org/10.1016/0045-7825\(96\)01019-5](https://doi.org/10.1016/0045-7825(96)01019-5)
 42. Izzuddin BA (1990) *Nonlinear dynamic analysis of framed structures*. Dissertation. Imperial College London
 43. Taylor GI (1948) The use of flat-ended projectiles for determining dynamic yield stress I. Theoretical considerations. *Proc R Soc Lond A* 194:289–299. <https://doi.org/10.1098/rspa.1948.0081>
 44. Bonet J, Burton AJ (1998) A simple average nodal pressure tetrahedral element for incompressible and nearly incompressible dynamic explicit applications. *Commun Numer Meth Eng* 14:437–449. [https://doi.org/10.1002/\(SICI\)1099-0887\(199805\)14:5%3c437::AID-CNMI62%3e3.0.CO;2-W](https://doi.org/10.1002/(SICI)1099-0887(199805)14:5%3c437::AID-CNMI62%3e3.0.CO;2-W)
 45. Simo JC, Armero F (1992) Geometrically non-linear enhanced strain mixed methods and the method of incompatible modes. *Mech Res Commun* 31:507–517. <https://doi.org/10.1016/j.mechrescom.2004.02.006>
 46. de Souza Neto EA, Perić D, Dutko M, Owen DRJ (1996) Design of simple low order finite elements for large strain analysis of nearly incompressible solids. *Int J Solids Struct* 33:3277–3296. [https://doi.org/10.1016/0020-7683\(95\)00259-6A](https://doi.org/10.1016/0020-7683(95)00259-6A)
 47. Love E, Sulsky DL (2006) An energy-consistent material-point method for dynamic finite deformation plasticity. *Int J Numer Meth Eng* 65:1608–1638. <https://doi.org/10.1002/nme.1512>

Publisher's Note Springer Nature remains neutral with regard to jurisdictional claims in published maps and institutional affiliations.